

Reversible and nonvolatile manipulation of the spin-orbit interaction in ferroelectric field-effect transistors based on a two-dimensional bismuth oxychalcogenide

Ming-Yuan Yan,^{1,3} Shuang-Shuang Li,² Jian-Min Yan,⁴ Li Xie,³ Meng Xu,⁵ Lei Guo,³ Shu-Juan Zhang,² Guan-Yin Gao,⁶ Fei-Fei Wang,⁷ Shan-Tao Zhang,¹ Xiaolin Wang,⁸ Yang Chai,⁴ Weiyao Zhao,^{8,*} and Ren-Kui Zheng^{3,9,*}

¹National Laboratory of Solid State Microstructures, College of Engineering and Applied Science & Jiangsu Key Laboratory of Artificial Functional Materials & Collaborative Innovation Center of Advanced Microstructures, Nanjing University, Nanjing 210093, China

² School of Materials Science and Engineering and Jiangxi Engineering Laboratory for Advanced Functional Thin Films, Nanchang University, Nanchang 330031, P. R. China

³ State Key Laboratory of High Performance Ceramics and Superfine Microstructure, Shanghai Institute of Ceramics, Chinese Academy of Sciences, Shanghai 200050, P. R. China

⁴Department of Applied Physics, The Hong Kong Polytechnic University, Hong Kong 999077, P. R. China

⁵College of Science, Hohai University, Nanjing 211189, P. R. China

⁶Hefei National Laboratory for Physical Sciences at the Microscale, University of Science and Technology of China, Hefei 230026, P. R. China

⁷Key Laboratory of Optoelectronic Material and Device, Department of Physics, Shanghai Normal University, Shanghai 200234, P. R. China

⁸Institute for Superconducting and Electronic Materials, & ARC Centre of Excellence in Future Low-Energy Electronics Technologies, Innovation Campus, University of Wollongong, NSW 2500, Australia

⁹School of Physics and Materials Science, Guangzhou University, Guangzhou 510006, P. R. China

*Correspondence to: weiyao.zhao@monash.edu (W.Y. Zhao) and zrk@ustc.edu (R.K. Zheng)

ABSTRACT: Spin-orbit interaction (SOI) offers a nonferromagnetic scheme to realize spin polarization through utilizing an electric field. Electrically tunable SOI through electrostatic gates have been investigated, however, the relatively weak and volatile tunability limit its practical applications in spintronics. Here, we demonstrate the nonvolatile electric-field control of SOI via constructing ferroelectric Rashba architectures, i.e., 2D Bi₂O₂Se/PMN-PT ferroelectric field effect transistors. The experimentally observed weak antilocalization (WAL) cusp in Bi₂O₂Se films implies the Rashba-type SOI that arises from asymmetric confinement potential. Significantly, taking advantage of the switchable ferroelectric polarization, the WAL-to-weak localization (WL) transition trend reveals the competition between spin relaxation and dephasing process, and the variation of carrier density leads to a reversible and nonvolatile modulation of spin relaxation time and spin splitting energy of Bi₂O₂Se films by this ferroelectric gating. Our work provides a scheme to achieve nonvolatile control of Rashba SOI with the utilization of ferroelectric remanent polarization.

1. Introduction

Spin-orbit interaction (SOI) has been intensively studied for related exotic physical phenomena and potential applications in spintronic devices and quantum computing fields [1-3]. SOI may result from either the lack of lattice inversion symmetry known as Dresselhaus effect, or Rashba type with broken structure symmetry imposed by external fields or asymmetric confinement potential [4,5]. Unlike traditional magnetic-field-induced spin polarization, SOI offers a nonferromagnetic scheme to realize the same purpose through utilizing an electric field.

And the effective modulation of SOI by electrostatic field have been explored in low-dimensional systems. However, the tunability of SOI through those dielectric gates are usually volatile and relatively weak, which is limited by the strength of electric field and low achievable areal charge densities $n_{2D} \sim 10^{12}-10^{13} \text{ cm}^{-2}$ [6-8].

Alternatively, ferroelectric (FE) materials with large spontaneous electric polarization can generate a strong local electric field, and modify the carrier densities of adjacent materials, thus leading to a greater tunability [9-11]. Moreover, ferroelectric gate can potentially tune the spin degree of freedom in a nonvolatile manner, which has been recently demonstrated in various spintronic devices, such as reversible and nonvolatile electrical switching of spin polarization and spin-charge conversion [12-16]. However, the nonvolatile manipulation of SOI involves replacing the dielectric gate by a ferroelectric one has been rarely reported so far. Thus, it is highly desired to realize a nonvolatile electric-field control of SOI using remanent polarization of ferroelectrics for the development of future spin memory and logic devices.

As an emerging 2D semiconductor material, the bismuth layered oxyselenide $\text{Bi}_2\text{O}_2\text{Se}$ is a good candidate for the modulation of SOI, which exhibits superior physical and chemical properties with a moderate band gap (0.8 eV), ultrahigh carrier mobility and good air stability [17-20]. Recently, some studies have reported excellent transport properties of $\text{Bi}_2\text{O}_2\text{Se}$, which stimulates further exploration of its novel quantum transport phenomena [19,21]. Therefore, it is of great significance to investigate the SOI in $\text{Bi}_2\text{O}_2\text{Se}$ system, which has been less experimentally studied until now. Moreover, the tetragonal crystal structure ($a = b = 3.89 \text{ \AA}$, $c = 12.21 \text{ \AA}$) of $\text{Bi}_2\text{O}_2\text{Se}$ enable it to be epitaxially grown on the widely used ferroelectric $\text{Pb}(\text{Mg}_{1/3}\text{Nb}_{2/3})\text{O}_3$ - PbTiO_3 (PMN-PT, $a \sim b \sim c \sim 4.02 \text{ \AA}$) single crystal [Figure 1(a)]. And the areal carrier density of

$\text{Bi}_2\text{O}_2\text{Se}$ ($n_{2\text{D}} \sim 10^{13} \text{ cm}^{-2}$) is lower than the $n_{2\text{D}} \sim 10^{14} \text{ cm}^{-2}$ resulting from the ferroelectric remanent polarization ($P_r \approx 25\text{-}40 \mu\text{C}/\text{cm}^2$) [10,19,22,23]. Hence, the 2D $\text{Bi}_2\text{O}_2\text{Se}/\text{PMN-PT}$ heterostructure would be a potential candidate system, in which the SOI of $\text{Bi}_2\text{O}_2\text{Se}$ could be reversibly and nonvolatily manipulated via interfacial polarization charges of ferroelectric PMN-PT.

In this paper, we have achieved nonvolatile manipulation of SOI through constructing ferroelectric Rashba architectures, i.e., $\text{Bi}_2\text{O}_2\text{Se}/\text{PMN-PT}$ 2D-FeFETs [Fig. 1(b)]. Different from tuning the interfacial spin-orbit coupling with ferroelectricity through the spin Hall angle, this work demonstrates the SOI tuning in $\text{Bi}_2\text{O}_2\text{Se}/\text{PMN-PT}$ heterostructure by magnetotransport method. Upon switching the direction of ferroelectric polarization, the *in situ* electric-field control of carrier density, resistance and magnetoresistance are realized by the ferroelectric field effect. Further magnetotransport measurements demonstrate the presence of a Rashba-type SOI in $\text{Bi}_2\text{O}_2\text{Se}$ films arising from the asymmetric confinement potential. The dependence of WAL to WL transition on polarization state, thickness, and temperature reveal that the crossover is determined by the relative scale of spin relaxation length and phase coherence length. Moreover, utilizing the ferroelectric gate, the SOI and spin-splitting energy could be modulated in a reversible and nonvolatile manner.

2. Experiments

$\text{Bi}_2\text{O}_2\text{Se}$ films were deposited on (001)-oriented PMN-PT single-crystal substrates by the pulse laser deposition (PLD) with a XeCl excimer laser ($\lambda = 308 \text{ nm}$). Before the deposition of films, the base pressure of the chamber was evacuated to a pressure lower than $5.0 \times 10^{-5} \text{ Pa}$. The working pressure was maintained at $3.0 \times 10^{-3} \text{ Pa}$ during film deposition process. Other preparation parameters like the target-to-substrate distance, laser energy density, substrate temperature, and pulse repetition rate were kept at 6 cm, $2 \text{ J}/\text{cm}^2$, 400 °C, and 3 Hz, respectively. After the

completion of deposition, the as-grown films were cooled naturally to room temperature.

Ag electrodes with a thickness of 100 nm were deposited on the top surface of Bi₂O₂Se films and the whole back of the bottom of PMN-PT substrates. The top Ag electrodes with different sizes are used to measure the electrical resistance and Hall resistance (Fig. S1 in the Supplemental Material [24]), respectively. The bottom Ag electrode together with one top Ag electrode was used to apply electric field to switch the polarization direction of the PMN-PT substrates.

The phase purity, out-of-plane and in-plane orientations, crystallinity of the grown films were analyzed by an x-ray diffractometer (PANalytical X'Pert PRO) equipped with CuK α_1 radiation ($\lambda=1.5406$ Å). The crystal structure and interface epitaxy of the prepared heterostructures were also characterized using a transmission electron microscope (Tecnai G2 F20 S-Twin). The surface morphology of Bi₂O₂Se films and piezoelectric properties of PMN-PT substrates were characterized via the atomic force microscopy (AFM) and piezoresponse force microscopy (PFM) using an atomic force microscope (MFP-3D, Asylum Research Inc.). The polarization-electric field (*P-E*) hysteresis loops of PMN-PT substrates were recorded by means of a TF3000 Ferroelectric Analyzer (aiXACCT, Germany) at room temperature. The electronic transport properties of Bi₂O₂Se films including the resistance, magnetoresistance, and carrier density were measured via the standard four-probe technique and the Van der Pauw method, respectively, using a physical property measurement system (PPMS) (Quantum Design).

3. Results and discussion

The x-ray diffraction (XRD) θ - 2θ scan pattern in Fig. 1(c) shows that (00*l*)-oriented (*l* = 4, 6, 8, 10) diffraction peaks are detected for the Bi₂O₂Se film, implying that the film is single phase

and c -axis oriented. The XRD rocking curve taken on the $\text{Bi}_2\text{O}_2\text{Se}$ (004) diffraction peak yields a full width at half maximum (FWHM) of 0.93° (Fig. S2 in the Supplemental Material [24]), indicating that the $\text{Bi}_2\text{O}_2\text{Se}$ film has a relatively high degree of crystallinity. The homogeneous distribution of Bi, O, and Se elements (Fig. S3 in the Supplemental Material [24]) and a relatively smooth surface with a root-mean-square (RMS) roughness of 4.5 nm shown by AFM image (Fig. S4(a) in the Supplemental Material [24]) further suggest the good quality of the $\text{Bi}_2\text{O}_2\text{Se}$ film. As depicted by the azimuthal ϕ scans in the inset of Fig. 1(c), the film and substrate both show a four-fold symmetry, which reveals that the $\text{Bi}_2\text{O}_2\text{Se}$ film grows epitaxially on the PMN-PT substrate. In addition, the epitaxial relationship is further confirmed by the HRTEM image. As shown in Fig. 1(d), a thickness of a ~ 4 nm $\text{Bi}_2\text{O}_2\text{Se}$ buffer layer is formed near the interface, and then the film grows layer by layer along the c -axis. The formation of the buffer layer is probably caused by the smaller lattice constant of $\text{Bi}_2\text{O}_2\text{Se}$ ($a \sim b \sim 0.39$ nm) than that of PMN-PT ($a \sim b \sim c \sim 0.40$ nm), in order to release the tensile strain accumulated at the beginning of film deposition. Afterwards, the lattice spacing of 0.39 and 1.22 nm correspond to the lattice parameter a (b) and c of the $\text{Bi}_2\text{O}_2\text{Se}$ unit cell, which manifests the well-defined atomic arrangement and epitaxial growth of the $\text{Bi}_2\text{O}_2\text{Se}$ film.

The superior ferroelectric properties of the PMN-PT (001) substrate are illustrated by the complete the PFM images [Figs. S4(b)-4(d) in the Supplemental Material [24]]. The shape of $\Delta R/R$ vs E curve in Fig. 1(e) is similar to that of the P - E loop of the PMN-PT [inset of Fig. 1(e)], implying that the ferroelectric field effect determines the resistance switching behaviors. Here, $\Delta R/R$ is defined as $\Delta R/R = [R(E) - R(0)]/R(0)$, where $R(E)$ and $R(0)$ are the resistance of the film with and without the application of external electric fields, respectively. After removing the electric field, a

maximum value $\sim 30\%$ of $\Delta R/R$ has been achieved for a 75-nm $\text{Bi}_2\text{O}_2\text{Se}$ film as the polarization state changes from P_r^- to P_r^+ at room temperature, where P_r^- and P_r^+ states represent the negative [top right inset in Fig. 1(f)] and positive [bottom left inset in Fig. 1(f)] polarization states of the PMN-PT substrate, respectively. Note that, the resistance relaxation behavior manifested by the non-square $\Delta R/R$ vs E curve [Fig. 1(e)] could be caused by the trapping effects of defect states in the 4-nm disordered interfacial layer [25].

The negative Hall coefficients in Fig. 1(f) show that the 75-nm $\text{Bi}_2\text{O}_2\text{Se}$ film is an n -type semiconductor whose majority charge carriers are electrons. The correspondingly calculated room temperature carrier densities n are $1.06 \times 10^{19} \text{ cm}^{-3}$ for the P_r^+ state and $0.81 \times 10^{19} \text{ cm}^{-3}$ for the P_r^- state, respectively. In addition, the *in situ* XRD θ - 2θ scan in Fig. 1(g) proves that the polarization reversal of PMN-PT does not affect the strain state of the film since the diffraction peaks of the $\text{Bi}_2\text{O}_2\text{Se}$ film remain unchanged. All these evidences confirm that the resistance change of $\text{Bi}_2\text{O}_2\text{Se}$ film is dominated by the ferroelectric field effect. As schematically illustrated by the bottom left inset in Fig. 1(f), with the PMN-PT positively poled, the negative polarization charges are induced at the interface between $\text{Bi}_2\text{O}_2\text{Se}$ and PMN-PT, which will attract holes from the film to the interface region. This increases the electron carrier density of $\text{Bi}_2\text{O}_2\text{Se}$ film, leading to the decrease of the resistance of the film. The situation for the P_r^- state is opposite by applying a negative electric field to PMN-PT (top right inset). Consequently, the nonvolatile and reversible modulation of resistance and carrier density have been realized in $\text{Bi}_2\text{O}_2\text{Se}/\text{PMN-PT}$ 2D-FeFETs.

The low-temperature electronic transport properties of $\text{Bi}_2\text{O}_2\text{Se}$ films with several representative thicknesses are studied. With decreasing film thickness, the measured volume carrier density decreases monotonously as shown in Figure 2(a), and the discrepancy of the carrier

density between the P_r^+ and P_r^- states become more pronounced. This suggests the more prominent modulation ability of the ferroelectric field effect as the films become thinner, consistent with the largest $\Delta R/R$ realized in the 75-nm film (Fig. S5 in the Supplemental Material [24]). On the other hand, the values of Ioffe-Regel parameter $k_{Fl} = (3\pi^2 n)^{2/3} \hbar \mu / e$, where \hbar is the reduced Planck constant and μ is the electron mobility (Fig. S6 in the Supplemental Material [24]), for different film thicknesses are obviously larger than one at low temperature ~ 200 K [Fig. 2(b)], implying that $\text{Bi}_2\text{O}_2\text{Se}$ films are in the weakly disordered regime at this temperature range [26,27].

The magnetoresistance (MR) of the $\text{Bi}_2\text{O}_2\text{Se}$ films in Fig. 2(c) exhibits a polarization-induced difference and show a similarly reduced magnitude of regulation with increasing film thickness. Here, MR is defined as $\text{MR} = [R(H) - R(0)]/R(0)$, $R(H)$ and $R(0)$ referring to the resistance in the presence and absence of a magnetic field H , respectively. As the film thickness increases, in the range of $H > 1$ T, the shape of MR varies from a parabola pointing downwards, to a double-dip W-shaped curve, finally to a parabola pointing upwards, along with the sign changing from negative to positive. This transition behavior of MR including the sign and magnitude is strongly influenced by different carrier density [28,29]. On the other hand, the MR of the 75-nm $\text{Bi}_2\text{O}_2\text{Se}$ film with increasing temperature in Fig. 2(d) and Figs. S7-S9 in the Supplemental Material [24] resembles the curve-shape transitions mentioned above. Particularly, a sharp cusp near zero-magnetic-field in the MR curve is observed at low temperatures. This is a characteristic signature of weak antilocalization (WAL) effect, which implies the presence of spin-orbit interaction (SOI) in the $\text{Bi}_2\text{O}_2\text{Se}$ films.

As an effective method to identify SOI, the low-field magnetoconductance behavior due to the weak localization (WL) and WAL have been extensively employed to investigate spin

relaxation processes in various systems [30]. For a 2D disordered system, the low-field WAL effect with different mechanisms can be described by the Iordanskii-Lyanda-Geller-Pikus (ILP) theory (Equation S1) or the Hikami-Larkin-Nagaoka (HLN) theory [31,32]. As the assumption is satisfied from the Ioffe-Regel parameter $k_{Fl} > 1$, the fittings of low-field magnetoconductance $\Delta G = G(H) - G(0) = R^{-1}(H) - R^{-1}(0)$ with both theories are shown in Figure 3. It is clear that the HLN fitting provides better agreement with the experimental data (Table S1), proving that the HLN theory is more effective to describe WAL in the Bi₂O₂Se film, consistent with the earlier literature [33]. Specially, the magnetoconductance of the WAL effect using HLN theory is given as below:

$$\Delta G(B) = -\frac{e^2}{\pi h} \left[\frac{1}{2} \Psi \left(\frac{B_\varphi}{B} + \frac{1}{2} \right) - \frac{1}{2} \ln \left(\frac{B_\varphi}{B} \right) + \Psi \left(\frac{B_{so} + B_{el}}{B} + \frac{1}{2} \right) - \ln \left(\frac{B_{so} + B_{el}}{B} \right) - \frac{3}{2} \Psi \left(\frac{(4/3)B_{so} + B_\varphi}{B} + \frac{1}{2} \right) + \frac{3}{2} \ln \left(\frac{(4/3)B_{so} + B_\varphi}{B} \right) \right] \quad (1)$$

Here, Ψ is the digamma function. Three subscripts φ , so and el denote inelastic dephasing process, spin-orbit scattering, and elastic scattering, respectively. The characteristic magnetic field B_φ , B_{so} and B_{el} could be extracted from the fitting to the experimental data. The mean free path $L_{el} = (\hbar/4eB_{el})^{1/2}$ (Fig. S12 in the Supplemental Material [24]) are much smaller than the distance between two top-top electrodes, and thus the carrier transport in Bi₂O₂Se films is in the diffusive regime [33].

In order to determine the strength of SOI, the low-field ΔG of the 75-nm Bi₂O₂Se film for the P_r^+ and P_r^- states are fitted and plotted in Figure 4(a) for the most notable WAL feature, and other ΔG data of films with different thicknesses are shown in (Figs. S10-S11 in the Supplemental Material [24]). At $T=3$ K, the observed sharp WAL peak of ΔG near zero field is caused by the positive correction to the conductance with the presence of SOI. With heating to 30 K, the sharp

peak is gradually suppressed and eventually develops into a broad dip, a signature of WL effect. Hence, the temperature dependent WAL-WL transition is observed here, as reported in previous trilayer Graphene, SrTiO₃-FETs, and InAs/GaSb double quantum well [34-36]. Intriguingly, upon the ferroelectric polarization switching from the P_r^+ state to the P_r^- state of PMN-PT substrate, the WAL effect is suppressed as reflected by the decrease in the magnitude of ΔG and a broaden of the WAL peak of the Bi₂O₂Se film, exhibiting a polarization-induced tendency from WAL to WL.

To investigate the spin relaxation and phase coherence process, temperature-dependent spin relaxation length L_{so} and dephasing length L_ϕ calculated from $L_{so,\phi} = (\hbar/4eB_{so,\phi})^{1/2}$ are plotted in Figs. 4(b) and 4(d), respectively. The L_ϕ show almost no dependence on the polarization states [Figs. 4(b)], and basically follow a power law of $L_\phi \sim T^{-0.5}$ [Figs. 4(c) and 4(e)]. This indicates that the dephasing process is primarily owing to the Nyquist scattering, i.e., electron-electron scattering with small energy transfers [37,38]. In contrast, the L_{so} presents a clear polarization-induced difference [Fig. 4(d)], which are attributed to the modulation of the carrier density by the ferroelectric field effect. The values of $L_{so} \sim 84$ nm for the P_r^+ state and ~ 102 nm for the P_r^- state at 3 K, shorter than ~ 290 nm in Al_xGa_{1-x}N/GaN 2DEG and ~ 250 nm in InSb nanowires, prove the presence of strong SOI in the Bi₂O₂Se film [39,40]. Here, because of the inherent inversion symmetry presented in Bi₂O₂Se, and given the electric-field induced polarization charges, therefore, the Rashba-type SOI is the most likely dominant mechanism in the 2D Bi₂O₂Se film, consistent with previous reports [41,42]. Remarkably, the polarization induced controllability of L_{so} is much stronger than the conventional dielectric gating effect in Bi₂O₂Se nanoplates [33]. These results significantly demonstrate ferroelectric gating control of the SOI in the

Bi₂O₂Se/PMN-PT system.

Furthermore, L_{so} and L_ϕ for the P_r^+ and P_r^- states are respectively plotted in Figs. 4(c) and 4(e), and show a crossover with increasing temperature. This nicely illustrates the key aspect that when the L_{so} is shorter than L_ϕ for $T < 15$ K, the WAL is observed because the spin precession destroys the phase coherence of electron wave function on time-reversed closed path; otherwise, the WL is dominant due to thermally enhanced dephasing process [43]. As the carrier density for the P_r^+ state is higher than that for the P_r^- state for the 75-nm film [Fig. 2(a)], this results in shorter L_{so} and larger L_ϕ/L_{so} for the P_r^+ state, which gives rise to the stronger WAL, as manifested by the sharper negative ΔG in Fig. 4(a). Consequently, the temperature corresponding to the intersection point between L_{so} and L_ϕ for the P_r^+ state is larger than that for the P_r^- state [Fig. 4(c) and 4(e)], consistent with the transition trend from WAL to WL in the ΔG curves. All these analyses fully prove that the WAL effect and Rashba-type SOI in Bi₂O₂Se film could be nonvolatily manipulated by switching the ferroelectric polarization.

Thickness-dependent magnetoconductance ΔG of the Bi₂O₂Se films with thicknesses ranging from 75 to 150 nm at 3 K are shown in Figure 5(a). All theoretical fittings with HLN theory to the experimental data are in good agreement. As the films become thicker, the characteristic WAL peak around zero magnetic field is gradually weakened, presenting a thickness-dependent WAL-WL crossover. Moreover, the derived spin relaxation length L_{so} , dephasing length L_ϕ and mean free path L_{el} basically decrease with increasing film thickness (Fig. S12 in the Supplemental Material [24]). As a result, L_ϕ gradually approaches to L_{so} in thicker films, leading to neglectable WAL effect in the 150-nm film [Fig. 5(a)]. And this is also reflected by the intersection point between L_{so} and L_ϕ shifting to lower temperature with increasing film thickness [Figs. 4(c) and 4(e) and (Figs. S10

and S11 in the Supplemental Material [24]). Thus, the stronger WAL effect and more effective manipulation of SOI through ferroelectric field effect is expected in thinner Bi₂O₂Se film whose carrier density could be more effectively modulated by ferroelectric polarization.

Significantly, the influences of the ferroelectric field effect on the phase and spin relaxation times are further elaborated. The phase relaxation time can be obtained by $\tau_\phi = \hbar/(4eDB_\phi)$, where the diffusion coefficient $D = v_F^2 \tau_{tr} / 2$ is calculated by the Fermi velocity $v_F = k_F \hbar / m^*$ and transport relaxation time $\tau_{tr} = \mu m^* / e$ with Fermi wave vector $k_F = (3\pi n)^{1/3}$ and effective electron mass $m^* = 0.184m_e$. As shown by Fig. 5(b), the temperature dependence of τ_ϕ scales as $\tau_\phi \sim T^{-1}$, which could be evidenced again that the Nyquist dephasing with electron-electron interaction is the main phase relaxation mechanism [37]. However, for thicker Bi₂O₂Se films, the variation trend of τ_ϕ vs T diverges from the dotted line $\sim T^{-1}$, which may originate from the deviation from the 2D nature. On the other hand, the spin relaxation time τ_{so} is given by $\tau_{so} = \hbar/(4eDB_{so})$. Taking the 75-nm film as an example, this yields a spin relaxation time $\tau_{so} \sim 9$ ps for the P_r^- state, much larger than $\tau_{so} \sim 4$ ps for the P_r^+ state (Table 1), due to the stronger SOI in the higher carrier density state [33,37]. Again, this result demonstrates the polarization-induced tunability of SOI upon switching the polarization state from P_r^- to P_r^+ .

Table 1. The values of transport parameters and SOI related parameters for 75-nm film at 3 K.

	n (cm ⁻³)	μ (cm ² V ⁻¹ s ⁻¹)	D (m ² /s)	L_{so} (nm)	L_ϕ (nm)	τ_{so} (ps)	Δ_{so} (meV)	β (eV Å ³)
P_r^+	1.56×10^{19}	133.33	0.0017	84.0	186.4	4.29	1.91	2.07
P_r^-	1.07×10^{19}	115.95	0.0011	102.2	195.4	9.35	1.38	2.18

Given that Rashba SOI contributes to band spin splitting, the corresponding spin splitting energy is calculated using $\Delta_{so} = \hbar/(2\tau_{tr} \tau_{so})^{1/2}$. Carrier density dependent Δ_{so} plotted in Fig. 5(d)

shows that Δ_{so} increases linearly with the carrier density for Bi₂O₂Se films with different thicknesses. This also supports that the dominant SOI mechanism is the Rashba-type [36]. Therefore, the Rashba coefficient β for SOI could be further obtained from $4\beta^2 k_F^6 = \Delta_{so}^2 = \frac{2e\hbar D}{\tau_{tr}} B_{so}$. The calculated value of β presents a systematic variation trend in relation to the carrier density [Fig. 5(e)], similar to some systems like 2DEG in SrTiO₃-FETs, 2D hole gas in gated diamond devices [35,38]. Notably, the values of Δ_{so} derived here, e.g., 1.3-1.9 meV for the 75-nm Bi₂O₂Se film (Table 1), exceed many other 2D systems in terms of magnitude [44,45]. More impressively, the nonvolatile modulation of Δ_{so} realized here through ferroelectric polarization is intrinsically different from those volatile one after removing electric field in dielectric gates.

Conclusions

In present work, the 2D Bi₂O₂Se films are epitaxially grown on ferroelectric PMN-PT (001) substrates to form Bi₂O₂Se/PMN-PT 2D-FeFETs. The *in situ* electric-field control of the carrier density, resistance, and magnetoresistance are realized by ferroelectric field effect. Further, the polarization state, film thickness, and temperature dependent WAL effect are systematically measured and analyzed. The low-field magnetoconductance of WAL with HLN fittings demonstrate the presence of a strong spin-orbit interaction in 2D Bi₂O₂Se films due to the asymmetric confinement potential. The crossover of WAL to WL is primarily determined by the relative scale of spin relaxation length and dephasing length, and the main phase relaxation mechanism is the Nyquist scattering. Remarkably, the modulation of spin-orbit interaction realized by ferroelectric gating is reversible and nonvolatile. Our work manifests that heterostructure

systems utilizing films with Rashba SOI and ferroelectric polarization could achieve reversible and nonvolatile manipulation of SOI, which may inspire schemes for spintronics and related quantum applications.

Acknowledgements

This work was supported by the National Natural Science Foundation of China (Grant No. 11974155). X.W. and W.Z. acknowledge the supporting form ARC Centre of Excellence in Future Low-Energy Electronics Technologies CE170100039.

References

- [1] K. C. Nowack, F. H. L. Koppens, Y. V. Nazarov, and M. K. Vandersypen, Coherent Control of a Single Electron Spin with Electric Fields, *Science* **318**, 1430 (2007).
- [2] A. Manchon, H. C. Koo, J. Nitta, S. M. Frolov, and R. A. Duine, New Perspectives for Rashba Spin-Orbit Coupling, *Nat. Mater.* **14**, 871 (2015).
- [3] W. Desrat, F. Giazotto, V. Pellegrini, M. Governale, and F. Beltram, Anticrossings of Spin-Split Landau Levels in an InAs Two-dimensional Electron Gas with Spin-orbit Coupling, *Phys. Rev. B* **71**, 153314 (2005).
- [4] G. Dresselhaus, Spin-Orbit Coupling Effects in Zinc Blende Structures, *Phys. Rev.* **100**, 580 (1955).
- [5] Y. A. Bychkov, and E. I. Rashba, Oscillatory Effects and The Magnetic Susceptibility of Carriers in Inversion Layers, *J. Phys. C* **17**, 6039 (1984).
- [6] A. T. Neal, H. Liu, J. Gu, and P. D. Ye, Magneto-Transport in MoS₂: Phase Coherence, Spin Orbit Scattering and the Hall Factor, *ACS Nano* **7**, 7077 (2013).
- [7] N. Hemsworth, V. Tayari, F. Telesio, S. Xiang, S. Roddaro, M. Caporali, A. Ienco, M. Serrano-Ruiz, M. Peruzzini, G. Gervais, T. Szkopek, and S. Heun, Dephasing in Strongly Anisotropic Black Phosphorus, *Phys. Rev. B* **94**, 245404 (2016).
- [8] E. Zhang, R. Chen, C. Huang, J. H. Yu, K. T. Zhang, W. Y. Wang, S. S. Liu, J. W. Ling, X. G. Wan, H. Z. Lu, and F. X. Xiu, Tunable Positive to Negative Magnetoresistance in Atomically Thin WTe₂, *Nano Lett.* **17**, 878 (2017).
- [9] J. M. Yan, Z. X. Xu, T. W. Chen, M. Xu, C. Zhang, X. W. Zhao, F. Liu, L. Guo, S. Y. Yan, G. Y. Gao, F. F. Wang, J. X. Zhang, S. N. Dong, X. G. Li, H. S. Luo, W. Y. Zhao, and R. K. Zheng, Nonvolatile and Reversible Ferroelectric Control of Electronic Properties of Bi₂Te₃ Topological Insulator Thin Films Grown on Pb(Mg_{1/3}Nb_{2/3})O₃-PbTiO₃ Single Crystals, *ACS Appl. Mater.*

[Interfaces](#) **11**, 9548 (2019).

[10] Q. X. Zhu, M. M. Yang, M. Zheng, R. K. Zheng, L. J. Guo, Y. Wang, J. X. Zhang, X. M. Li, H. S. Luo, and X. G. Li, Ultrahigh Tunability of Room Temperature Electronic Transport and Ferromagnetism in Dilute Magnetic Semiconductor and PMN-PT Single-Crystal-Based Field Effect Transistors via Electric Charge Mediation, [Adv. Funct. Mater.](#) **25**, 1111 (2015).

[11] M. Y. Yan, J. M. Yan, M. Y. Zhang, T. W. Chen, G. Y. Gao, F. F. Wang, Y. Chai, and R. K. Zheng, Nonvolatile Manipulation of Electronic and Ferromagnetic Properties of NiO-Ni Epitaxial Film by Ferroelectric Polarization Charge, [Appl. Phys. Lett.](#) **117**, 232901 (2020).

[12] D. Pantel, S. Goetze, D. Hesse, and M. Alexe, Reversible electrical switching of spin polarization in multiferroic tunnel junctions, [Nat. Mater.](#) **11**, 289-293 (2012).

[13] D. Sun, M. Fang, X. Xu, L. Jiang, H. Guo, Y. Wang, W. Yang, L. Yin, P. C. Snijders, and T. Z. Ward, Active control of magnetoresistance of organic spin valves using ferroelectricity. [Nat. Commun.](#) **5**, 4396 (2014).

[14] W. Lin, W. N. Lin, S. D. Pollard, R. Guo, Heng, Y. Yoong, S. H. Chen, H. Wang, L. Liu, C. J. Li, X. J. Yu, J. X. Xiao, X. Chi, J. H. Yu, J. Zhou, T. J. Zhou, H. Yang, and J. S. Chen, Tuning of current-induced effective magnetic field through Rashba effect engineering in hybrid multiferroic structures. [NPG Asia Mater.](#) **10**, 740-748 (2018).

[15] K. Cai, M. Yang, H. Ju, S. Wang, Y. Ji, B. Li, K. W. Edmonds, Y. Sheng, B. Zhang, N. Zhang, S. Liu, H. Zheng and K. Wang, Electric field control of deterministic current-induced magnetization switching in a hybrid ferromagnetic/ferroelectric structure. [Nat. Mater.](#) **16**, 712-716 (2017).

[16] N. Paul, T. Felix, V. A. Luis M., B. Julien, C. V. Diogo, G. Vincent, F. Stéphane, B. Agnès, V. Laurent, B. Manuel, and A. Jean-Philippe, Non-volatile electric control of spin-charge conversion in a SrTiO₃ Rashba system. [Nat.](#) **580**, 483-486 (2020).

[17] J. X. Wu, Y. J. Liu, Z. J. Tan, C. W. Tan, J. B. Yin, T. R. Li, T. Tu, and H. L. Peng, Chemical Patterning of High-Mobility Semiconducting 2D Bi₂O₂Se Crystals for Integrated Optoelectronic Devices, [Adv. Mater.](#) **29**, 1704060 (2017).

[18] J. X. Wu, C. W. Tan, Z. J. Tan, Y. J. Liu, J. B. Yin, W. H. Dang, M. Z. Wang, and H. L. Peng, Controlled Synthesis of High-Mobility Atomically Thin Bismuth Oxyselenide Crystals. [Nano Lett.](#) **17**, 3021 (2017).

[19] J. X. Wu, H. T. Yuan, M. M. Meng, C. Chen, Y. Sun, Z. Y. Chen, W. H. Dang, C. W. Tan, Y. J. Liu, J. B. Yin, Y. B. Zhou, S. Y. Huang, H. Q. Xu, Y. Cui, H. Y. Hang, Z. F. Liu, Y. L. Chen, B. H. Yan, and H. L. Peng, High Electron Mobility and Quantum Oscillations in Non-encapsulated Ultrathin Semiconducting Bi₂O₂Se, [Nat. Nanotechnology](#) **12**, 530 (2017).

[20] Y. Liang, Y. J. Chen, Y. W. Sun, S. P. Xu, J. X. Wu, C. W. Tan, X. F. Xu, H. T. Yuan, L. X. Yang, Y. L. Chen, P. Gao, J. D. Guo, and H. L. Peng, Molecular Beam Epitaxy and Electronic Structure of Atomically Thin Oxyselenide Films, [Adv. Mater.](#) **31**, 1901964 (2019).

[21] Y. Y. Lv, L. Xu, S. T. Dong, Y. C. Luo, Y. Y. Zhang, Y. B. Chen, S. H. Yao, J. Zhou, Y. S. Cui, S. T. Zhang, M. H. Lu, and Y. F. Chen, Electron-electron Scattering Dominated Electrical and Magnetotransport Properties in The Quasi-Two-Dimensional Fermi Liquid Single-Crystal Bi₂O₂Se,

[Phys. Rev. B](#) **99**, 195143 (2019).

[22] X. W. Zhao, S. N. Dong, G. Y. Gao, Z. X. Xu, M. Xu, J. M. Yan, W. Y. Zhao, Y. K. Liu, S. Y. Yan, J. X. Zhang, Y. Wang, H. Z. Lu, X. G. Li, J. K. Furdyna, H. S. Luo, and R. K. Zheng, Reversible and Nonvolatile Manipulation of the Electronic Transport Properties of Topological Insulators by Ferroelectric Polarization Switching, [npj Quantum Materials](#) **3**,52 (2018).

[23] S. E. Park, and T. R. Shrout, Ultrahigh Strain and Piezoelectric Behavior in Relaxor Based Ferroelectric Single Crystals, [J. Appl. Phys.](#) **82**, 1804 (1997).

[24] See Supplemental Material at [link](#) for Fitting of ILP theory; The low-field magnetoconductance fitted with HLN and ILP theory; Schematic configuration of R and hall measurements; The RC taken on the $\text{Bi}_2\text{O}_2\text{Se}$ (004) diffraction peak; The BSE image and elemental mapping of Bi, O and Se elements taken on the 75-nm $\text{Bi}_2\text{O}_2\text{Se}$ film; The AFM image of the 100-nm $\text{Bi}_2\text{O}_2\text{Se}$ film and out-of-plane PFM images of different polarization states of a PMN-PT substrate; The $\Delta R/R$ with 75 nm, 100 nm, 150 nm as a function of electric field E applied to PMN-PT substrates; Temperature dependence of Hall mobility of $\text{Bi}_2\text{O}_2\text{Se}$ films with different thicknesses for the P_r^+ and P_r^- states of PMN-PT; The MR of different thickness $\text{Bi}_2\text{O}_2\text{Se}$ film for P_r^+ and P_r^- states of PMN-PT under different temperatures; WAL effect in the 100-nm and 150-nm $\text{Bi}_2\text{O}_2\text{Se}$ film spin; The L_ϕ , L_{so} and L_{el} as a function of temperature of $\text{Bi}_2\text{O}_2\text{Se}$ films with different thicknesses for the P_r^+ and P_r^- states of PMN-PT.

[25] Z. X. Xu, J. M. Yan, M. Xu, L. Guo, T. W. Chen, G. Y. Gao, S. N. Dong, M. Zheng, J. X. Zhang, Y. Wang, X. G. Li, H. S. Luo, and R. K. Zheng, Integration of Oxide Semiconductor Thin Films with Relaxor-Based Ferroelectric Single Crystals with Large Reversible and Nonvolatile Modulation of Electronic Properties, [ACS Appl. Mater. Interfaces](#) **10**, 32809 (2018).

[26] G. Bergmann, Weak Localization in Thin Films, [Phys. Rep.](#) **107**, 1 (1984).

[27] J. Liao, Y. Ou, X. Feng, S. Yang, C. Lin, W. Yang, K. Wu, K. He, X. Ma, Q. K. Xue, and Y. Li, Observation of Anderson Localization in Ultrathin Films of Three-Dimensional Topological Insulators, [Phys. Rev. Lett.](#) **114**, 216601 (2015).

[28] Q. Y. Xu, L. Hartmann, H. Schmidt, H. Hochmuth, M. Lorenz, R. S. Grund, C. Sturm, D. Spemann, and M. Grundmann, Metal-Insulator Transition in Co-doped ZnO: Magnetotransport Properties, [Phys. Rev. B](#) **73**, 205342 (2006).

[29] Q. Y. Xu, L. Hartmann, H. Schmidt, H. Hochmuth, M. Lorenz, and D. Spemann, s-d Exchange Interaction Induced Magnetoresistance in Magnetic ZnO, [Phys. Rev. B](#) **76**, 134417 (2007).

[30] R. Wang, R. S. Deacon, J. Yao, C. M. Lieber, and K. Ishibashi, Electrical modulation of weak antilocalization and spin-orbit interaction in dual gated Ge/Si core/shell nanowires, [Semicond. Sci. Technol.](#) **32**, 094002 (2017).

[31] S. Hikami, A. I. Larkin, and Y. Nagaoka, Spin-Orbit Interaction and Magnetoresistance in the Two-Dimensional Random System, [Prog. Theor. Phys.](#) **63**, 707 (1980).

[32] S. V. Iordanskii, Y. B. Lyanda-Geller, and G. E. Pikus, Weak Localization in Quantum Wells with Spin-Orbit Interaction, [JETP Lett.](#) **60**, 206 (1994).

[33] M. M. Meng, S. Y. Huang, C. W. Tan, J. X. Wu, Y. M. Jing, H. L. Peng, and H. Q. Xu, Strong Spin-Orbit Interaction and Magnetotransport in Semiconductor $\text{Bi}_2\text{O}_2\text{Se}$ Nanoplates, [Nanoscale](#)

[10, 2704 \(2018\)](#).

- [34] Z. Y. Chen, H. T. Yuan, Y. F. Zhang, K. Nomura, T. Gao, Y. B. Gao, H. Shimotani, Z. F. Liu, Y. Iwasa, Tunable spin-Orbit interaction in trilayer graphene exemplified in electric-double-layer transistors, [Nano Lett. **12**, 2212-2216 \(2012\)](#).
- [35] H. Nakamura, T. Koga, and T. Kimura, Experimental Evidence of Cubic Rashba Effect in an Inversion-Symmetric Oxide, [Phys. Rev. Lett. **108**, 206601 \(2012\)](#).
- [36] V. Sazgari, G. Sullivan, and I. I. Kaya, Interaction-Induced Crossover Between Weak Antilocalization and Weak Localization in a Disordered InAs/GaSb Double Quantum Well, [Phys. Rev. B **101**, 155302 \(2020\)](#).
- [37] C. Niu, G. Qiu, Y. X. Wang, Z. C. Zhang, M. W. Si, W. Z. Wu, and P. D. Ye, Gate-Tunable Strong Spin-orbit Interaction in Twodimensional Tellurium Probed by Weak-Antilocalization, [Phys. Rev. B **101**, 205414 \(2020\)](#).
- [38] G. Akhgar, O. Klochan, L. Beveren, M. T. Edmonds, F. Maier, B. J. Spencer, J. C. McCallum, L. Ley, A. R. Hamilton, and C. I. Pakes, Strong and Tunable Spin-Orbit Coupling in a Two-Dimensional Hole Gas in Ionic-Liquid Gated Diamond Devices, [Nano Lett. **16**, 3768 \(2016\)](#).
- [39] N. Thillosen, S. Cabanas, N. Kaluza, V. A. Guzenko, H. Hardtdegen, and T. Schapers, Weak Antilocalization in Gate-Controlled $\text{Al}_x\text{Ga}_{1-x}\text{N}/\text{GaN}$ Two-Dimensional Electron Gases, [Phys. Rev. B **73**, 241311 \(2006\)](#).
- [40] I. vanWeperen, B. Tarasinski, D. Eeltink, V. S. Pribiag, S. R. Plissard, E. P. A. M. Bakkers, L. P. Kouwenhoven, and M. Wimmer, Spin-Orbit Interaction in InSb Nanowires, [Phys. Rev. B **91**, 201413 \(2015\)](#).
- [41] J. Ying, J. He, G. Yang, M. Liu, Z. Lv, X. Zhang, H. Liu, K. Zhao, R. Jiang, Z. Ji, J. Fan, C. Yang, X. Jing, G. Liu, X. Cao, X. Wang, L. Lu, and F. Qu, Magnitude and Spatial Distribution Control of the Supercurrent in $\text{Bi}_2\text{O}_2\text{Se}$ -Based Josephson Junction, [Nano Lett. **20**, 2569 \(2020\)](#).
- [42] S. V. Eremeev, Y. M. Koroteev, and E. V. Chulkov, Surface Electronic Structure of Bismuth Oxychalcogenides, [Phys. Rev. B **100**, 115417 \(2019\)](#).
- [43] H. Yuan, M. S. Bahramy, and B. J. Yang, Zeeman-type Spin Splitting Controlled by an Electric Field, [Nat. Phys. **9**, 563 \(2013\)](#).
- [44] G. M. Minkov, A. A. Sherstobitov, A. V. Germanenko, O. E. Rut, V. A. Larionova, and B. N. Zvonkov, Antilocalization and Spin-Orbit Coupling in the Hole Gas in Strained $\text{GaAs}/\text{In}_x\text{Ga}_{1-x}\text{As}/\text{GaAs}$ Quantum Well Heterostructures, [Phys. Rev. B **71**, 165312 \(2005\)](#).
- [45] R. Moriya, K. Sawano, Y. Hoshi, S. Masubuchi, Y. Shiraki, A. Wild, C. Neumann, G. Abstreiter, D. Bougeard, T. Koga, and T. Machida, Cubic Rashba Spin-Orbit Interaction of a Two-Dimensional Hole Gas in a Strained-Ge/SiGe Quantum Well, [Phys. Rev. Lett. **113**, 086601 \(2014\)](#).

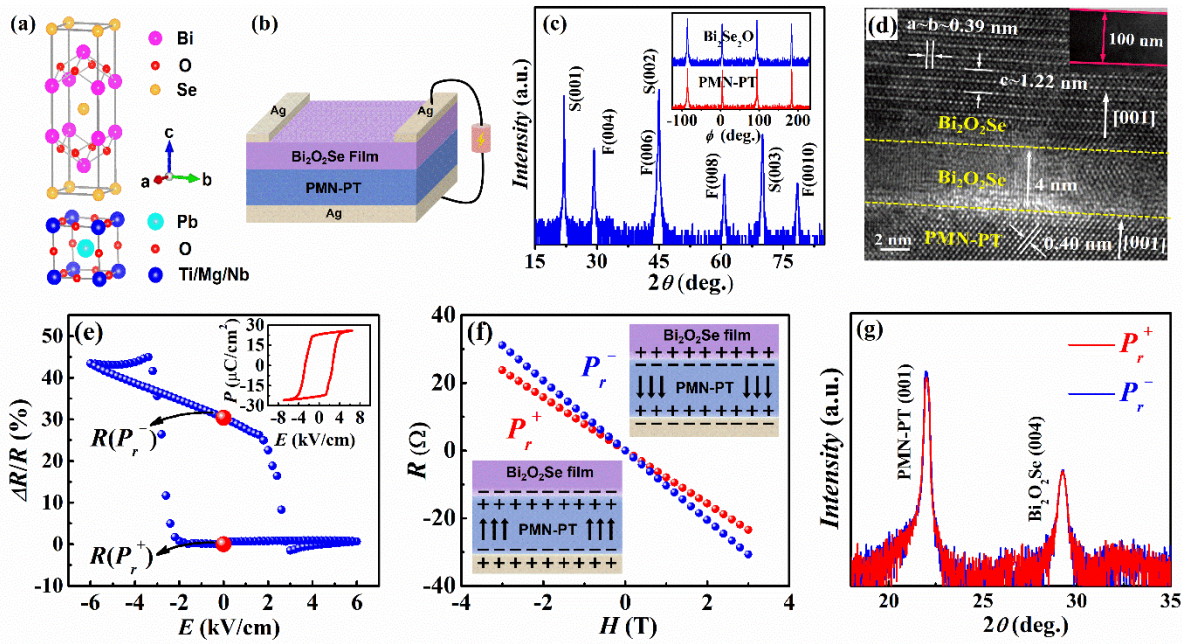


FIG. 1. (a) Crystal structure of tetragonal Bi₂O₂Se and pseudocubic PMN-PT. (b) Schematic diagram of the Bi₂O₂Se/PMN-PT 2D-FET device. (c) XRD θ - 2θ scan and ϕ scan patterns (inset) for the Bi₂O₂Se/PMN-PT heterostructure. Here, F and S represent the Bi₂O₂Se film and PMN-PT substrate, respectively. (d) TEM image taken on the interface of a 100-nm Bi₂O₂Se/PMN-PT. (e) The relative resistance change ($\Delta R/R$) of the 75-nm Bi₂O₂Se film as a function of electric field E applied to PMN-PT, the inset showing ferroelectric polarization versus electric field (P - E) loop of PMN-PT (001). (f) Room temperature Hall resistance of the 75-nm Bi₂O₂Se film versus magnetic field when PMN-PT was in the positive (P_r^+) and negative (P_r^-) poled states, respectively, and schematic illustration for the accumulation of positive (top right inset) and negative (bottom left inset) polarization charges under P_r^+ and P_r^- states of PMN-PT. (g) XRD θ - 2θ scan pattern of the Bi₂O₂Se film for the P_r^+ and P_r^- states of PMN-PT.

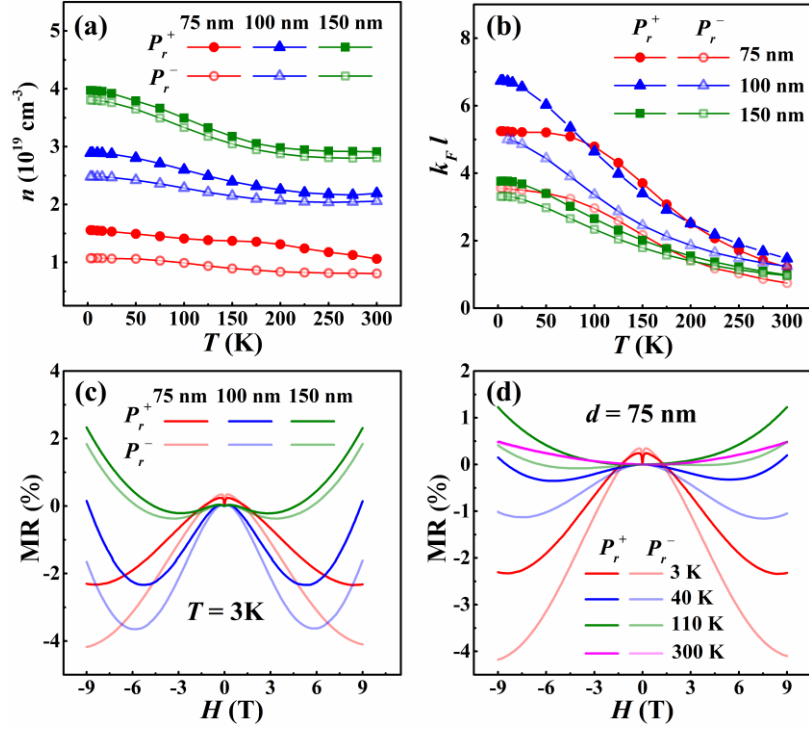


FIG. 2. (a) Temperature dependence of the carrier density of Bi₂O₂Se films with different thicknesses. (b) Temperature dependence of the Ioffe-Regel parameter (k_{FI}) of Bi₂O₂Se films with different thicknesses. (c) Magnetic field dependent magnetoresistance (MR) of the Bi₂O₂Se films with different thicknesses at 3 K. (d) Magnetic field dependent MR of the 75-nm Bi₂O₂Se film at various fixed temperatures.

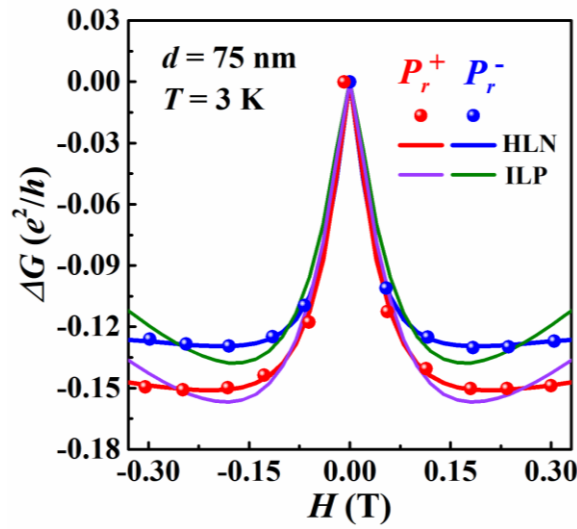


FIG. 3. Experimental WAL data of the 75-nm Bi₂O₂Se film for the P_r^+ and P_r^- states of PMN-PT, as measured at $T=3$ K. The solid lines are fitted with different theories (red and blue line for the HLN theory, purple and green line for the ILP theory).

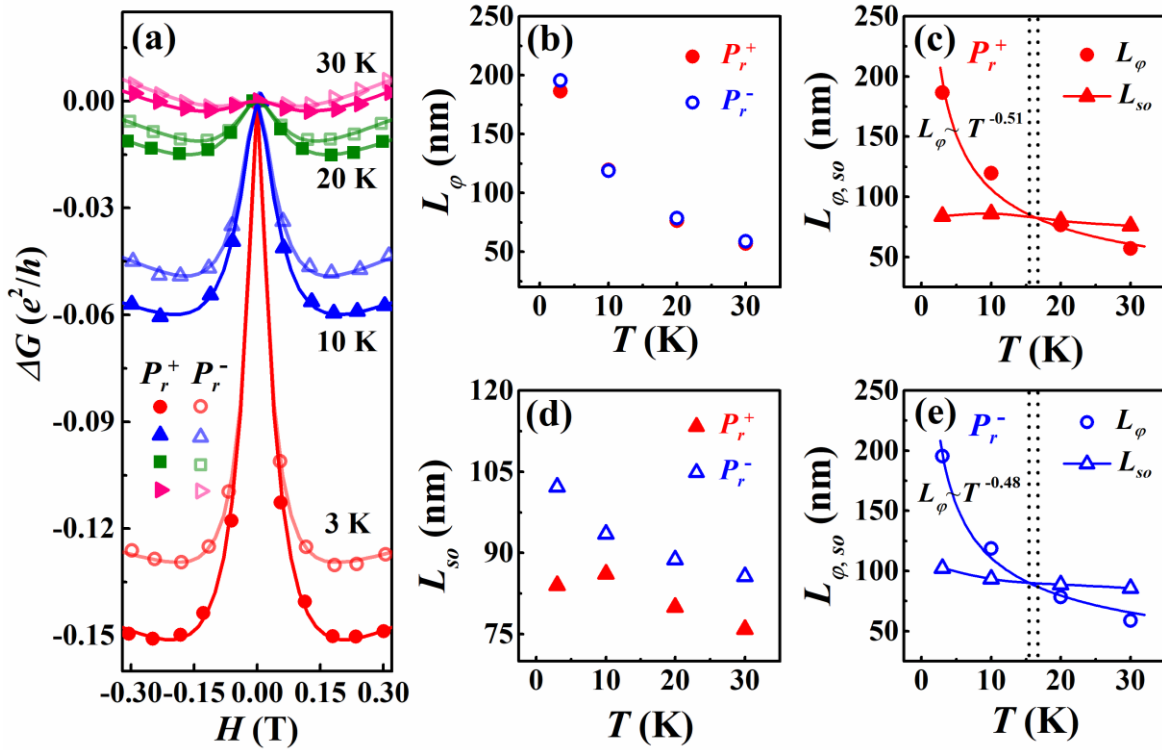


FIG. 4. (a) Low-field magnetoconductance ΔG (e^2/h) of the 75-nm Bi₂O₂Se film for the P_r^+ and P_r^- states at

different fixed temperatures. The solid lines represent the fitting results obtained with HLN equation. (b) Dephasing length (L_ϕ) and (d) spin relaxation length (L_{so}) as a function of temperature, extracted from the $\Delta G(e^2/h)$ data for the P_r^+ and P_r^- states. Characteristic L_{so} and L_ϕ involved in WAL and WL as a function of temperature for (c) P_r^+ and (e) P_r^- states, and specially, the solid lines for L_ϕ in (c) and (e) are the fits to experimental data by power function.

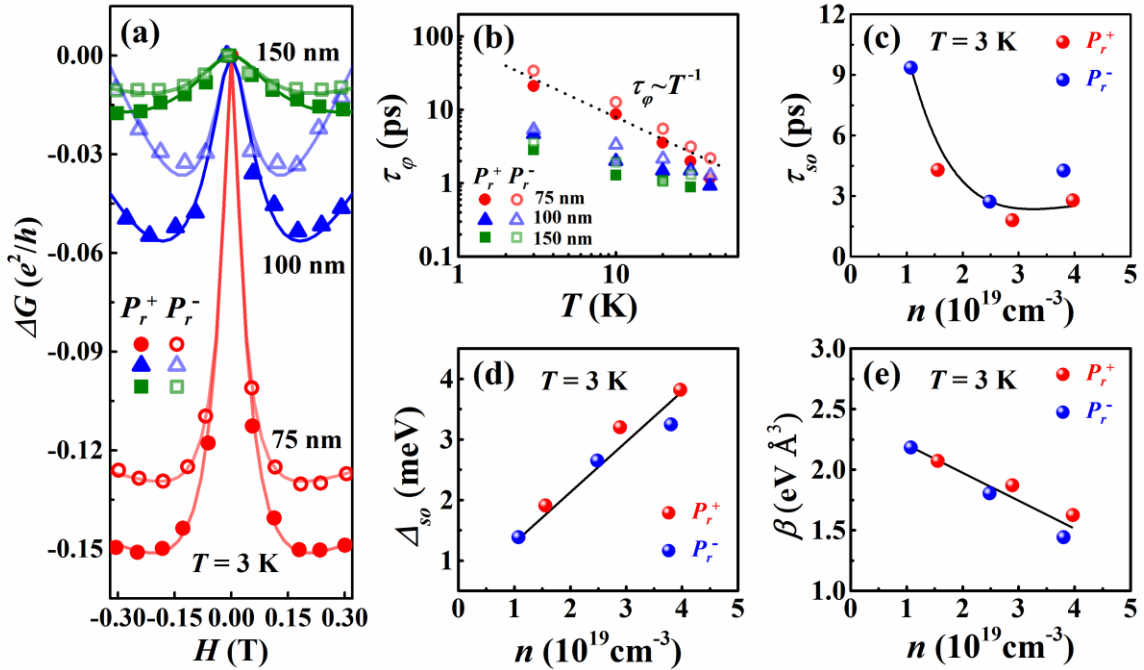


FIG. 5. (a) Magnetoconductance of $\text{Bi}_2\text{O}_2\text{Se}$ films with different thicknesses for the P_r^+ and P_r^- states of PMN-PT. The solid lines show fittings of experimental data with HLN equation. (b) Temperature dependence of phase relaxation time τ_ϕ of $\text{Bi}_2\text{O}_2\text{Se}$ films with different thicknesses, the dotted line to signify $\tau_\phi \sim T^{-1}$ for Nyquist

dephasing. (c) Spin relaxation time τ_{so} as a function of carrier density, the line is a guide to the eye. (d) Variation of the spin-orbit splitting energy Δ_{so} with the volume carrier density n . (e) Carrier density dependent Rashba coefficient β . The solid lines in (d) and (e) are linear fits to the data.